coatings

Article

Multi-Objective Process Optimization of Laser Cladding Co-Based Alloy by Process Window and Grey Relational Analysis

Haitao Yue [1,2], Ning Lv [1], Chenguang Guo [1,2,*], Jianhua Zhai [1,2], Weibing Dai [1,2], Jianzhuo Zhang [1,2] and Guochao Zhao [1,2]

[1] School of Mechanical Engineering, Liaoning Technical University, Fuxin 123000, China; yuehaitao@lntu.edu.cn (H.Y.); ln18004186969@163.com (N.L.)
[2] Liaoning Provincial Key Laboratory of Large-Scale Mining Equipment, Fuxin 123000, China
* Correspondence: guochenguang@lntu.edu.cn; Tel.: +86-15004183690

Abstract: To determine the optimal process parameters for the preparation of a Co-based alloy cladding layer, the experimental research of laser cladding Co-based alloy was carried out based on the optimal process window and grey relational analysis methods with 42CrMo as the substrate. The analysis of variance (ANOVA) was used to explore the influence laws of laser process parameters on the forming characteristics of the cladding layer within the optimal process window range. Furthermore, the optimal process parameter combination was obtained by grey relational analysis, and the experimental verification of the optimization results was conducted. It was found that the process parameter interval determined by the optimal process window was laser power 1300–2100 W, scanning speed 6–14 mm/s, and powder feeding rate 17.90–29.84 g/min. The influence order of each process parameter was: laser power > scanning speed > powder feeding rate. The optimal process parameters of laser power 2100 W, scanning speed 6 mm/s, and powder feeding rate 17.90 g/min were obtained. The experimental verification results of optimal process parameters proved that the grey correlation grade of the optimized parameters was improved by 0.260 compared with the initial parameters and agreed well with the prediction value with an accuracy of 96%. After optimization, the cross-sectional area, the ratio of the width to height, cladding efficiency, and powder utilization rate of the cladding track increased by 4.065 mm^2, 1.031, 19.032, and 70.3%, respectively, and the fluctuation ratio decreased by 60.9%. The optimal cladding track was well bonded to the substrate without cracks, holes, and evident element segregation, and included the phases of Cr_3C_7, CoCx, fcc-Co, and WC.

Keywords: laser cladding; co-based alloy; parameters optimization; process window; grey relational analysis

Citation: Yue, H.; Lv, N.; Guo, C.; Zhai, J.; Dai, W.; Zhang, J.; Zhao, G. Multi-Objective Process Optimization of Laser Cladding Co-Based Alloy by Process Window and Grey Relational Analysis. *Coatings* **2023**, *13*, 1090. https://doi.org/10.3390/coatings13061090

Academic Editor: Sae Chae Jeoung

Received: 23 May 2023
Revised: 7 June 2023
Accepted: 8 June 2023
Published: 13 June 2023

1. Introduction

Laser cladding is a green advanced surface modification technology that utilizes a high-energy-density laser beam to rapidly melt and solidify the cladding powder and substrate, forming a metallurgical bonding [1–3]. It is widely used in mining machinery [4], aerospace [5,6], railway [7,8], and other industrial fields because of its advantages such as small heat-affected zone, low dilution rate, and fast processing speed. As a layer-by-layer additive manufacturing technology, the final forming quality and service performance of the cladding layer largely depends on the geometrical characteristic and the fusion relationship of cladding tracks. Therefore, ensuring the production of a single cladding track with high forming quality and ideal performance is essential for laser additive manufacturing of parts.

The unreasonable selection of laser process parameters such as laser power, scanning speed, and powder feeding rate is the main reason for the poor forming characteristics of

the cladding layer [9]. Scholars have carried out a lot of research on various methods to optimize the process parameters of laser cladding, including the response surface method (RSM) [10–12], grey relational analysis [13,14], optimization algorithm [15], and linear regression method, etc. [16–18]. It was found that optimizing processing parameters is an effective way to improve the forming characteristics of the cladding layer. Gao et al. [10] and Meng et al. [11] adopted RSM to propose the regression models between laser process parameters and responses considering the cladding layer's forming characteristics and mechanical properties. They found that the scanning speed and laser power have the most significant effect on the dilution rate. In contrast, the scanning speed is the most remarkable parameter affecting microhardness and the ratio of cladding layer width to height. Wu et al. [12] optimized the process parameters of laser cladding Ni60A-25% WC on 42CrMo substrate surface by RSM. They obtained that the cladding layer has a dense microstructure and high mechanical properties under the optimal process parameters, in which microhardness is obviously higher compared with the substrate. Xu et al. [13] analyzed the influence of process parameters on the mechanical properties of the Inconel718 cladding layer by ANOVA. The optimal combination of process parameters related to the maximum microhardness, load value, and yield strength was obtained with grey correlation analysis. Deng et al. [14] studied the influence of laser power, scanning speed, and shielding gas flow rate on the responses of cladding height, cladding width, and dilution, etc. The multi-objective parameters were optimized by Taguchi-grey relational analysis method. The grey correlation value increased by 0.229 under optimal conditions. Guo et al. [15] established a multi-objective optimization model based on the maximum cladding height and cross-section area, minimum heat-affected zone area, and dilution rate, and further optimized the solution by the MOPSO algorithm. They concluded that the model has higher prediction accuracy, in addition, the scanning speed and powder feeding rate had a significant influence on the dilution rate and the geometric characteristics of the cladding layer. Razavi et al. [16–18] systematically studied the geometry of Inconel718, Ti-6Al-4V, and Co-Cr-Mo alloy cladding layers using linear regression, respectively. They drew the process map based on the model results to predict the influence of process parameters on the cladding layer geometry. Compared with the previous research, the current work pays more attention to the application of intelligent optimization algorithms.

42CrMo steel has favorable strength, hardness, and service characteristics as a common material for key parts of fully mechanized mining equipment [19]. It is extremely easy to produce wear, corrosion, and other failure behavior since it has been in a complex and harsh working environment. Co-based alloy cladding powder owes excellent self-melting, wear, corrosion, and oxidation resistance [20]. Therefore, scholars generally achieve surface modification by laser cladding technology on the surface of the damaged substrate with Co-based alloy powder. Cui et al. [21] used laser cladding technology to investigate the microstructure evolution of the cladding layer between the substrate and Co base alloy, and established that the overlap zone has positive corrosion resistance and no pitting behavior. Yang et al. [22] comprehensively explored the microstructure, hardness, corrosion, and wear behavior of Co-base alloy, and the results indicated that the cladding layer was well formed without visible defects. Combined with the analysis of laser process parameters, they obtained the corrosion resistance and wear resistance of the cladding layer significantly improved with the hardness increased.

From the current research results, scholars mainly focus on the related research on the service performance of the Co-based cladding layer. Compared with selective laser melting, the complicated and interactive physical phenomena including heat transfer, rapid solidification, terrible atmosphere, and fierce convective flow of laser cladding, result in additional difficulty in controlling the forming quality. Meanwhile, single-track cladding provides necessary information closely related to the formation mechanism of multi-layer and multi-track cladding. However, synthetically considering the forming quality, cladding efficiency and cost economy of the cladding layer, the more effective optimization of process parameters of the Co-based cladding layer is rarely reported.

In this study, the Co-based alloy single cladding track was prepared on the 42CrMo substrate surface based on Laser cladding technology. Firstly, the optimal process window was constructed, and the range of process parameters was optimized by an all-factor experiment. Secondly, the effect trend of laser power, scanning speed, and powder feeding rate on cross-section area, heat affected zone area, cladding efficiency, powder utilization rate, the ratio of cladding track width to height, and fluctuation ratio were further determined by ANOVA. Finally, the optimal process parameter combination was obtained by combining the gray relational analysis method. Furthermore, the effectiveness of parameters optimization in improving the forming characteristics, processing efficiency, and cost economy of the cladding layer was verified by experiments. The development of the research will have an important guiding significance for the preparation of a Co-based alloy cladding layer with excellent forming quality.

2. Materials and Methods

2.1. Experimental Materials and Equipment

In this research, the 42CrMo substrate was cut into 150 mm × 150 mm × 10 mm cube samples by wire cutting equipment. The samples were successively polished with 100–2000 # abrasive paper to ensure smoothness and remove the substrate oxidation layer before laser cladding treatment. Then, the surface impurities were cleaned with anhydrous ethanol and acetone, and dried for use. The cladding material adopted the spherical Co-based alloy powder with a diameter range of 45–150 μm. The particle characteristics and the elemental composition of Co-based alloy powder and 42CrMo substrate are shown in Figure 1a. The laser cladding processing system is presented in Figure 1b. It is composed of a fiber laser (LDM-3000, Laserline, Germany) (a continuous wavelength of 900–1080 nm, an output power of 100–3000 W, a laser spot of 4 mm, and a focal distance of 40 mm), a 6-axes industrial robot (KR30HA, KUKA, Germany), a coaxial powder feeding system, a water cooling system and a gas supply system (99% high purity argon used as powder carrier gas and shielding gas flow of 5 L/min and 10 L/min, respectively).

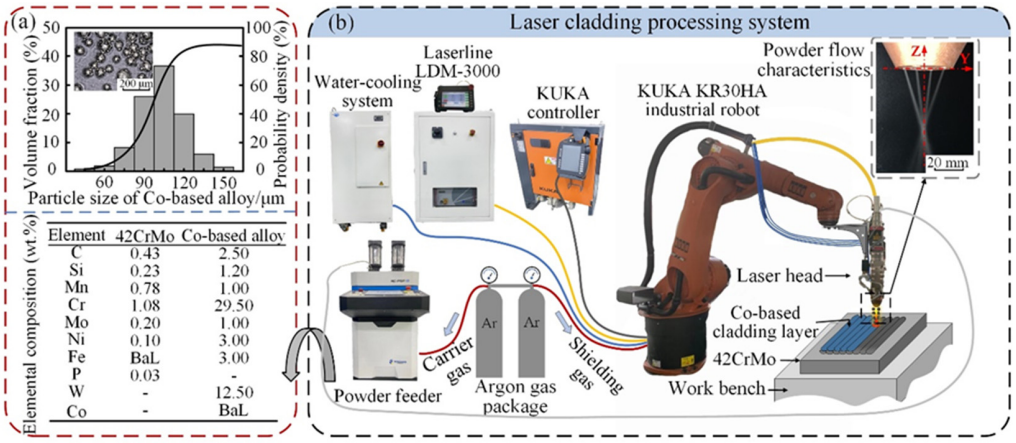

Figure 1. Experimental material and processing equipment of laser cladding: (**a**) Characteristic of cladding powder and elemental composition of the Co-based alloy and 42CrMo substrate; (**b**) Laser cladding processing system.

The samples surface characteristics of the cladding track were measured with a digital optical microscope (VHX-5000, Keyence, Japan). After cutting, grinding, polishing, corrosion (C_2H_5OH:HNO_3 = 24:1, vol.%), cleaning, and drying, the cladding tracks cross-section microstructure characteristics were observed by VHX-5000. The elemental composition and distribution of the Co-based alloy cladding layer were characterized by a field emission scanning electron microscope (Sigma 300, Zeiss, Germany) equipped with an EDAX spectrometer. The cladding layer phase composition was measured by Bruker D8 Ad-

vance X-ray diffractometer test platform (voltage 30 kV, electric current 10 mA, the Cu-Kα radiation, and scanning speed 5°/min).

2.2. Experimental Design

The cross-section geometric characteristics of a single cladding track are shown in Figure 2, including cladding height (H), cladding width (W), the cross-section area of (A_c), and heat-affected zone area (A_{HAZ}). To obtain a Co-based alloy single cladding track with excellent forming characteristics, cladding efficiency, and powder utilization rate, the laser power P, scanning speed V_s and powder feeding rate V_f were chosen as experimental factors. The all-factor experimental scheme of three factors and five levels is designed, as shown in Table 1.

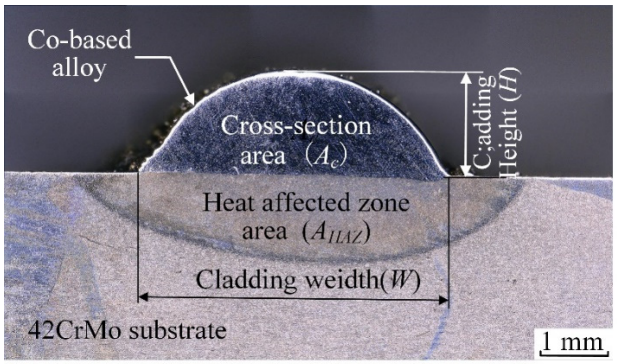

Figure 2. Cross-section geometric characteristics of the single cladding track.

Table 1. All-factor experimental design scheme.

Level	Laser Power P (W)	Scanning Speed V_s (mm/s)	Powder Feeding Rate V_f (r/min)
1	500	6	11.94
2	900	10	17.90
3	1300	14	23.87
4	1700	18	29.84
5	2100	22	35.81

3. Results and Discussion

3.1. Optimal Process Window

Figure 3 presents the five states (no fusion, lack of fusion, warping, rough and irregular, regular and smooth) marked with different colors under different process parameters for the 125 cladding tracks [23]. When Laser power is 500 W and 900 W, the laser energy is much lower than the melting point of the Co-based alloy powder and the 42CrMo substrate, leading to the formation of the cladding track being nonexistent. When the laser power and scanning speed increase to 1300 W and 18 mm/s, respectively, the lack of fusion appears due to the insufficient energy of the laser-irradiated molten pool. With the increase of laser power, the energy absorbed by the powder also increases accordingly, and the morphology of the cladding track gradually becomes continuous and smooth. However, when the scanning speed reaches 22 mm/s, the time for the powder to absorb laser power is insufficient, resulting in a rough and irregular surface of the cladding track. Meanwhile, as the powder feeding rate increases, the warpage occurs at both ends of the cladding track. The warpage phenomenon is severe when the powder feeding rate increases to 35.81 g/min. Thus, the effective process range of the laser cladding Co-based cladding layer is $P > 900$ W; $P = 1300$ W, $V_s < 8$ mm/s and $P = 1700$ W, $V_s < 22$ mm/s.

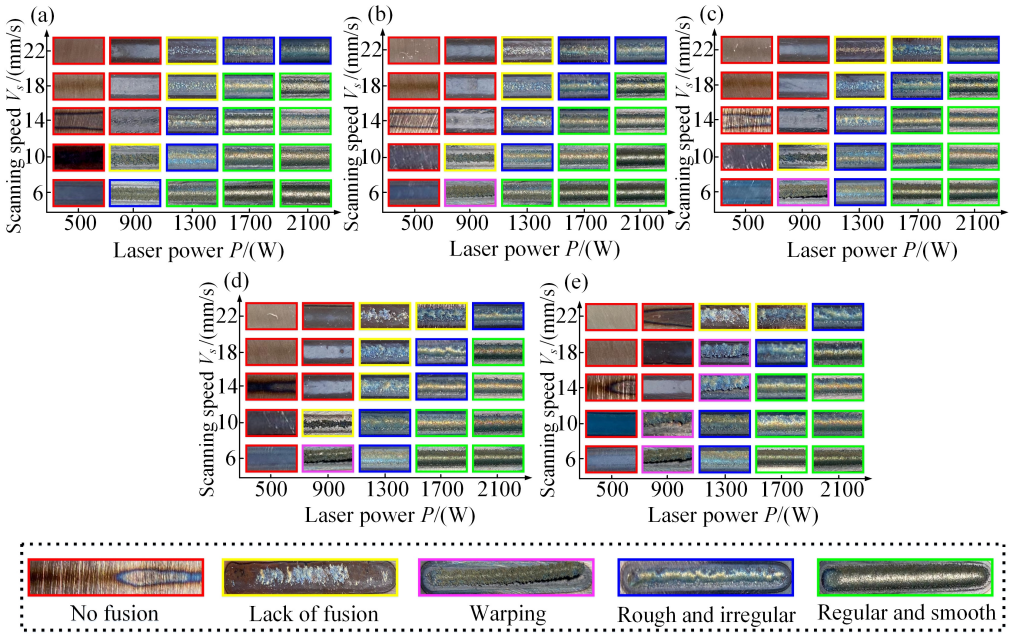

Figure 3. Morphology characteristics of cladding layers under different process parameters: (**a**) V_f = 11.94 g/min; (**b**) V_f = 17.90 g/min; (**c**) V_f = 23.87 g/min; (**d**) V_f = 29.84 g/min and (**e**) V_f = 35.81 g/min.

Considering the forming characteristics, processing efficiency, and cost economy of the single cladding track, the cross-section area A_c, cladding efficiency η_c, and powder utilization rate η_p are selected as evaluation indexes. The variation of the cladding track cross-section area Ac under different process parameters is shown in Figure 4. Laser power and scanning speed have a more significant impact on the cross-section area of the cladding track. When the laser power remained stable, the time of laser acting on the powder was shortened with the increase of the scanning speed, making it difficult for the powder to melt completely, and the cladding track cross-section area decreased obviously. When the laser power is 1300 W, the scanning speed has the most significant effect on the cladding track cross-section area. With the increase of laser power, when the scanning speed exceeds 10 mm/s, the cross-section area decreases slowly. In addition, the variation of powder feeding speed has no evident effect on the cladding track cross-section area. While the powder feeding speed is over 23.87 g/min, the cladding track cross-section area tends to be stable because the effective powder melting amount reaches the threshold.

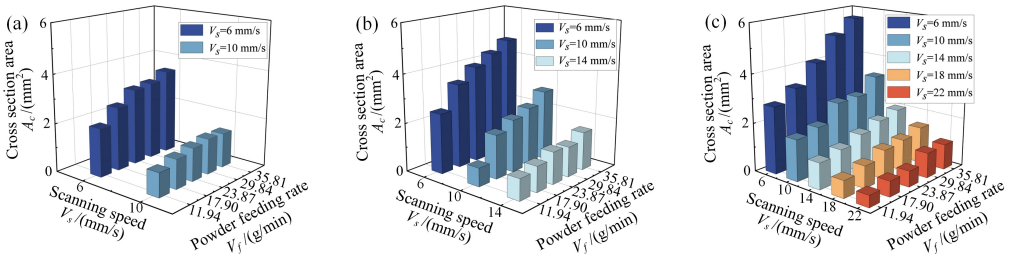

Figure 4. Influence of different process parameters on cross-section area: (**a**) P = 1300 W; (**b**) P = 1700 W and (**c**) P = 2100 W.

Cladding efficiency η_c is defined as the effective cladding volume of Co-based alloy powder per unit time [24], which is expressed as Equation (1). Comparing Figure 5a–c, it can be found that the laser power is the most influential parameter on the cladding efficiency. As the laser power increases, the influence of scanning speed on cladding efficiency tends to slow down because the scanning speed is negatively correlated with the

time of laser action on the powder. When the laser power is low to 1300 W, the cladding efficiency increases with the decrease in scanning speed on account that the powder has enough melting time. As shown in Figure 5b, when the laser power increases to 1700 W, the effect of scanning speed on the cladding efficiency begins to attenuate due to the increase of the energy of laser irradiated powder. In this case, the impact of powder feeding rate on the cladding efficiency becomes remarkable. This is because when the laser energy is sufficient, the powder involved in melting increases with the increase of powder feeding amount, and the cladding efficiency increases steadily. With the further growth of laser power, the trend of cladding efficiency increase is more prominent. Adequate laser energy at a higher powder feeding rate is spent in melting the Co-based alloy powder increasing the cladding efficiency. Meanwhile, with the further increase of laser power, the improvement trend of cladding efficiency is particularly significant, as presented in Figure 5c.

$$\eta_c = A_c \times V_s \tag{1}$$

where A_c is the cladding layer cross-section area, V_s is the scanning speed.

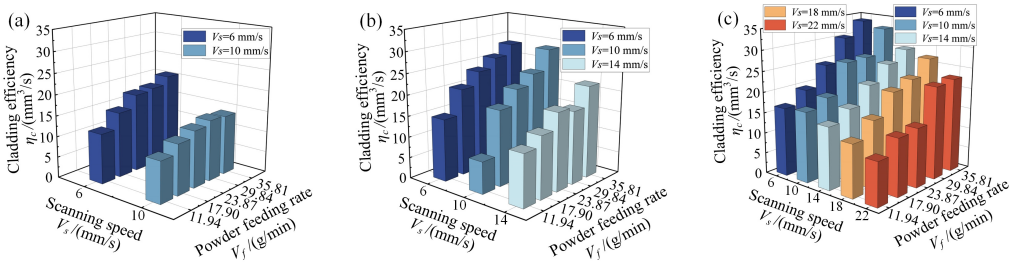

Figure 5. Influence of different process parameters on cladding efficiency: (**a**) P = 1300 W; (**b**) P = 1700 W and (**c**) P = 2100 W.

The powder utilization rate is defined as the ratio of the actual powder mass used in each cladding track to the powder feeding amount at the same time. From Figure 6, the two ends of the cladding track are assumed to be partially spherical according to the spatial structure characteristics of the cladding track in this research. Additionally, the powder utilization rate is calculated by Equation (2). The relationship between powder utilization rate and process parameters is noted in Figure 7. With the increase in the scanning speed, the powder utilization rate follows a decreasing trend with the same laser power. While with the increase in the laser power, the influence of scanning speed on the powder utilization rate gradually weakens. Until the laser power reaches 2100 W, as observed in Figure 7c, the powder utilization rate remains almost unchanged much with the variation in scanning speed and powder feeding rate. Obviously, the powder utilization remains higher due to more powder being melted with sufficient laser energy. Moreover, the effect of powder feeding rate on powder utilization rate followed the opposite trend with respect to the laser power. Because the amount of powder involved in melting is limited by laser energy, the number of unmelted powder increase at a higher powder feeding rate. In this study, powder utilization is minimal in case of the powder feed rate is up to the maximum of 35.81 g/min.

$$\eta_p = \frac{\rho_c\left\{lW + \pi/3H^2\left[3\left(W^2 + 4H^2\right)/8H - H\right]\right\}}{(l/V_s/60)V_f} \tag{2}$$

where ρ_c is cladding layer density, Co-based cladding layer density is 8.46 g/cm^3 in this study, l is cladding track processing length, l = 40 mm.

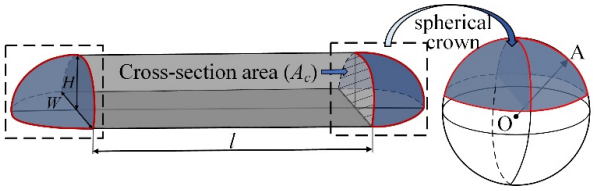

Figure 6. Schematic diagram of the spatial structure characteristics of the cladding track.

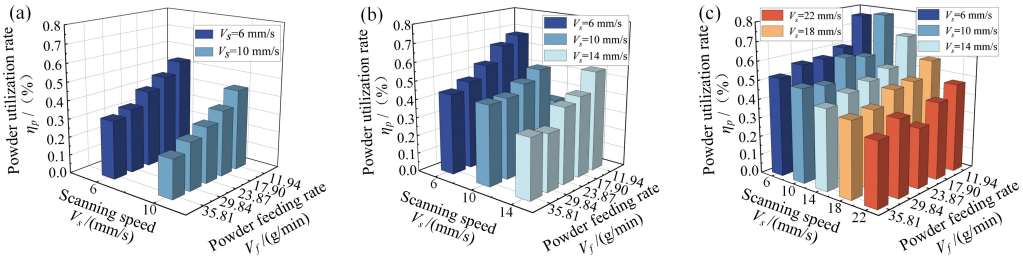

Figure 7. Influence of different process parameters on powder utilization rate: (**a**) P = 1300 W, (**b**) P = 1700 W, and (**c**) P = 2100 W.

Comprehensively considering the forming quality, processing efficiency, and cost economy of the cladding layer, the satisfactory morphological characteristics, cladding efficiency above 15 mm^3/s, and powder utilization higher than 50% cladding track are selected. The optimal range of process parameters is determined by laser power 1300–2100 W, scanning speed 6–14 mm/s, and powder feeding rate 17.90–29.84 g/min. From Figure 8, the optimal process window of the laser cladding Co-based alloy cladding layer is constructed based on the optimization ranges of process parameters.

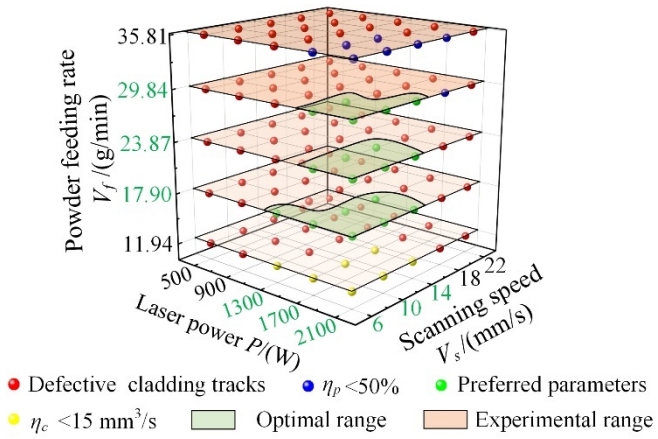

Figure 8. Optimal process window.

3.2. Multi-Objective Process Optimization

In order to obtain the optimal combination of process parameters, the process parameters are further optimized based on the above optimal process range. The design factors, levels, and scheme of the Taguchi orthogonal experiment using $L_{25}(5^3)$ are presented in Tables 2 and 3. Considering the forming characteristics of the Co-based alloy cladding layer, the thermal damage degree of the 42CrMo substrate, the wettability, the surface smoothness, the processing efficiency, and the cost economy. Cross-section area (A_c), heat affected zone area (A_{HAZ}), cladding efficiency (η_c), powder utilization rate (η_p), the ratio of cladding track width to height ($\lambda_{W/H}$), and fluctuation ratio (λ_f) are chosen as experimental responses. Where $\lambda_{W/H}$ is the ratio of the cladding width to the cladding height, λ_f is used to evaluate the smoothness of the cladding track (d is the fixed length that the intermediate

stationary stage of the cladding track, d = 20 mm), which the measurement and calculation methods are shown in Figure 9 and Equation (3).

$$\lambda_f = \frac{S_2}{S_1 + S_2} \tag{3}$$

where S_1 is the stationary region area and S_2 is the fluctuating region area within the cladding track fixed length d.

Table 2. $L_{25}(5^3)$ Orthogonal experimental factors and levels.

Level	Laser Power P (W)	Scanning Speed V_s (mm/s)	Powder Feeding Rate V_f (r/min)
1	1300	6	17.90
2	1500	8	20.88
3	1700	10	23.87
4	1900	12	26.85
5	2100	14	29.84

Table 3. $L_{25}(5^3)$ Taguchi orthogonal experimental design.

No.	P (W)	V_s (mm/s)	V_f (g/min)	No.	P (W)	V_s (mm/s)	V_f (g/min)
1#	1300	6	17.90	14#	1700	12	17.90
2#	1300	8	20.88	15#	1700	14	20.88
3#	1300	10	23.87	16#	1900	6	26.85
4#	1300	12	26.85	17#	1900	8	29.84
5#	1300	14	29.84	18#	1900	10	17.90
6#	1500	6	20.88	19#	1900	12	20.88
7#	1500	8	23.87	20#	1900	14	23.87
8#	1500	10	26.85	21#	2100	6	29.84
9#	1500	12	29.84	22#	2100	8	17.90
10#	1500	14	17.90	23#	2100	10	20.88
11#	1700	6	23.87	24#	2100	12	23.87
12#	1700	8	26.85	25#	2100	14	26.85
13#	1700	10	29.84				

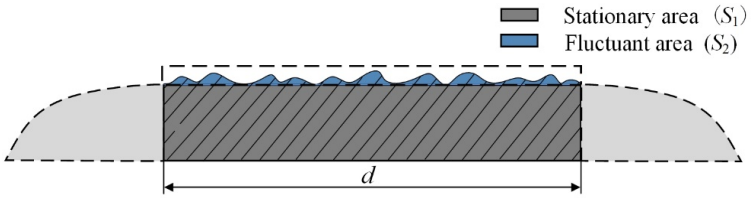

Figure 9. Schematic diagram of the longitudinal section for the cladding track.

Figure 10 shows the cross-section metallographic morphology of cladding tracks. It can be seen that the cladding quality of the cladding track is relatively satisfactory without apparent defects such as pores, cracks, no fusion, or warpage, and the cladding layers are well bonded with the substrate. Whereas the morphology characteristics and geometric size of each cladding track cross-section exist significant differences. The measurement results of each response for all specimens are listed in Table 4, in which some defect cladding tracks such as 2#–5#, 8#–10#, 13#–15#, 19#–20#, and 25# present irregular cross-section morphology and small cross-section area. Therefore, it is necessary to optimize the process parameters further.

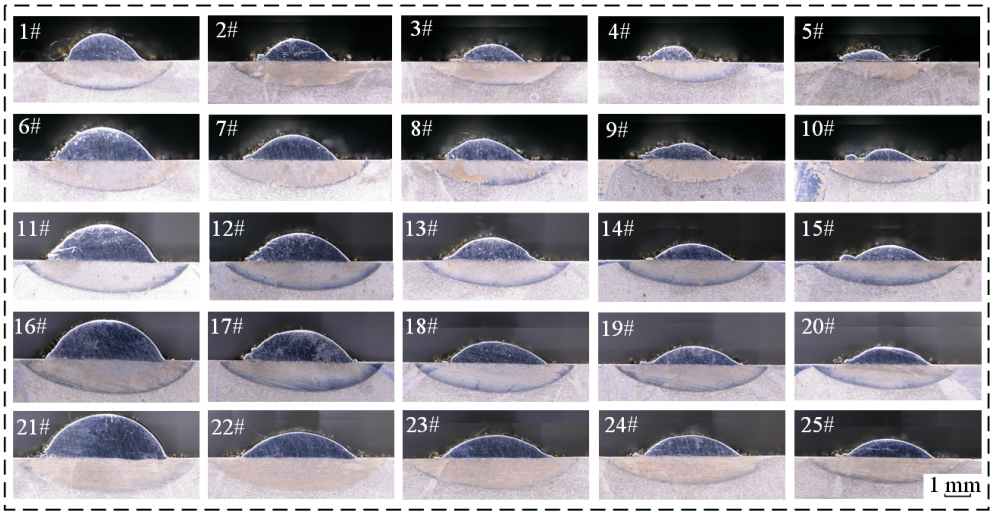

Figure 10. Cross-section morphology of cladding layers under different process parameters.

Table 4. Experimental results of each response for all specimens.

No.	A_c (mm^2)	A_{HAZ} (mm^2)	$\lambda_{W/H}$	λ_f (%)	η_c (mm^3/s)	η_p (%)
1#	2.64	4.60	3.37	27.03	15.84	47.89
2#	1.11	3.76	4.17	40.27	8.88	22.61
3#	0.89	3.26	4.76	49.30	8.90	19.71
4#	0.65	2.37	3.34	55.20	7.80	15.23
5#	0.67	1.90	3.54	80.47	9.38	16.47
6#	3.56	5.30	3.31	16.29	21.36	55.87
7#	2.55	4.46	3.55	24.91	20.40	46.23
8#	1.77	3.72	4.48	35.20	17.70	35.57
9#	1.42	3.08	4.28	40.34	17.04	30.40
10#	0.62	3.10	5.35	54.97	8.68	25.54
11#	4.4	5.72	3.05	12.27	26.40	60.03
12#	3.09	4.87	3.39	21.36	24.72	49.70
13#	2.33	4.14	4.03	27.61	23.30	42.31
14#	1.21	3.88	5.21	39.22	14.52	43.44
15#	1.02	4.09	4.59	41.41	14.28	36.17
16#	5.29	6.25	3.08	8.05	31.74	64.93
17#	3.79	5.34	3.54	18.21	30.32	55.46
18#	2.08	4.93	4.74	28.07	20.80	62.64
19#	1.67	4.52	4.88	31.43	20.04	51.40
20#	1.31	4.00	5.22	40.85	18.34	41.09
21#	6.34	7.23	2.89	13.81	38.04	70.46
22#	3.13	6.55	4.39	18.75	25.04	76.18
23#	2.6	5.76	4.86	21.05	26.00	67.54
24#	1.93	4.89	4.84	31.25	23.16	52.09
25#	1.23	4.27	5.25	38.22	17.22	34.10

3.2.1. Subsubsection

To reduce the unpredictable errors of experimental results due to the variability of original data caused by uncontrollable noise factors, a practical data analysis method is introduced: the signal-to-noise ratio (*SNR*) [25], which is an evaluation criterion for the sensitivity of the cladding layer-forming characteristics to noise factors. The larger the *SNR*, the more significant the impact on the response. The experimental objective is converted into the highest *SNR* for each response result. In general, the *SNR* is calculated by selecting corresponding formulas in Equation (4), which includes the larger the better (*LTB*, containing A_c, $\lambda_{W/H}$, η_c, and η_p), smaller the better (*STB*, containing A_{HAZ} and λ_f) and

nominal the better (*NTB*), and the *SNR* calculated results for each response are listed in Table 5.

$$SNR = \begin{cases} -10\log\left(\frac{1}{n}\sum_{i=1}^{n}\frac{1}{y_i^2}\right) & LTB \\ -10\log\left(\frac{1}{n}\sum_{i=1}^{n}y_i^2\right) & STB \\ -10\log\left(\frac{1}{n}\sum_{i=1}^{n}(y_i - m)^2\right) & NTB \end{cases} \quad (4)$$

where *SNR* is the signal-to-noise ratio of each response, n is the number of experiments per group (n = 1), y_i is the response value of experiment i (i = 1, 2, 3 . . . 25).

Table 5. *SNR* for each response.

No.	*SNR*					
	A_c	A_{HAZ}	$\lambda_{W/H}$	λ_f	η_c	η_p
1#	8.432	−13.255	10.542	11.361	23.995	−6.395
2#	0.906	−11.504	12.396	7.900	18.968	−12.913
3#	−1.012	−10.264	13.551	6.144	18.988	−14.104
4#	−3.742	−7.495	10.473	5.161	17.842	−16.344
5#	−3.479	−5.5751	10.973	1.887	19.444	−15.668
6#	11.029	−14.486	10.384	15.759	26.592	−5.056
7#	8.131	−12.987	11.008	12.072	26.193	−6.701
8#	4.959	−11.411	13.028	9.069	24.959	−8.977
9#	3.046	−9.771	12.632	7.886	24.629	−10.343
10#	−4.152	−9.8272	14.565	5.197	18.770	−11.855
11#	12.869	−15.148	9.683	18.223	28.432	−4.432
12#	9.799	−13.751	10.599	13.410	27.861	−6.072
13#	7.347	−12.34	12.108	11.178	27.347	−7.470
14#	1.656	−11.777	14.336	8.131	23.239	−7.242
15#	0.172	−12.234	13.229	7.657	23.095	−8.832
16#	14.469	−15.918	9.757	21.888	30.032	−3.752
17#	11.573	−14.551	10.978	14.793	29.635	−5.120
18#	6.361	−13.857	13.523	11.035	26.361	−4.063
19#	4.454	−13.103	13.759	10.054	26.038	−5.781
20#	2.345	−12.041	14.357	7.777	25.268	−7.725
21#	16.042	−17.183	9.216	17.196	31.605	−3.041
22#	9.911	−16.325	12.858	14.540	27.973	−2.363
23#	8.299	−15.208	13.725	13.534	28.299	−3.409
24#	5.711	−13.786	13.704	10.103	27.295	−5.665
25#	1.798	−12.609	14.410	8.354	24.721	−9.345

Based on the above Taguchi orthogonal experiment of $L_{25}(5^3)$, the impact of process parameters on each response result is further analyzed by adopting ANOVA [26–28], and the confidence intervals for the following ANOVA are all 95% [14]. Table 6 shows the ANOVA results for the cladding track cross-section area and the heat-affected zone area. It can be seen that the p-value of each process parameter in the cladding track cross-section area is all less than 0.05. Therefore, the laser power, scanning speed, and powder feeding rate have a significant effect on the cladding track cross-section area [29], which is because the laser power, scanning speed, and powder feeding rate determine the energy absorption amount of the powder, the time of the powder absorbing energy and the melting number of the powder. Similarly, the p-values for laser power and scanning speed in the heat-affected zone area are both less than 0.05, as laser power and scanning speed are the main factors influencing the amount of energy absorbed per unit of time in the substrate, followed by the powder feeding rate. The rank order of the process parameters and main effect plots are shown in Table 6 and Figure 11, and it can be concluded that the influence order of each parameter on the cladding track cross-section area and the heat-affected zone area are: $V_s > P > V_f$ and $P > V_s > V_f$. Meanwhile, the largest layer cross-section area and

the smallest heat-affected zone area can be obtained under the combination of process parameters $P5V_s1V_f5$ and $P1V_s5V_f5$, respectively.

Table 6. ANOVA results of A_c and A_{HAZ}.

Source	A_c					A_{HAZ}				
	P	***V_s***	***V_f***	**Error**	**Total**	***P***	***V_s***	***V_f***	**Error**	**Total**
DF	4	4	4	12	24	4	4	4	12	24
Seq SS	10.873	37.750	3.087	1.545	53.255	19.328	18.138	0.570	0.531	38.567
Adj SS	10.873	37.750	3.087	1.545		19.328	18.138	0.570	0.531	
Adj MS	2.718	9.438	0.772	0.129		4.832	4.535	0.143	0.044	
F-value	21.12	73.31	6.00			109.25	102.53	3.22		
p-value	0.000	0.000	0.007			0.000	0.000	0.052		

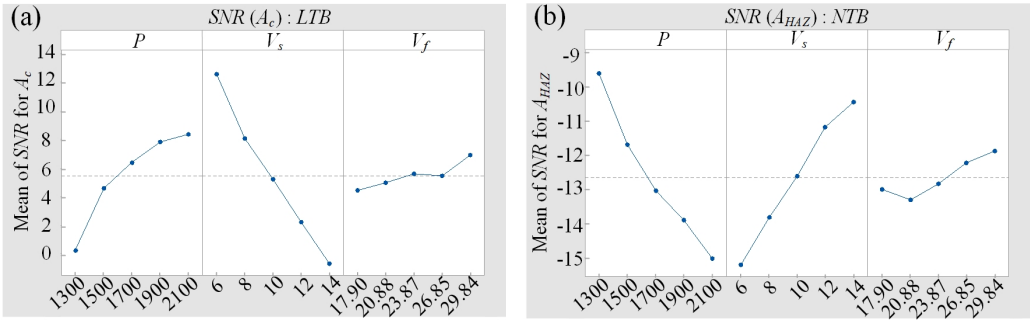

Figure 11. Main effect plots for the *SNR* analysis of (**a**) A_c and (**b**) A_{HAZ}.

Table 7 shows the ANOVA results for the ratio of cladding track width to height and fluctuation ratio. It can be clearly observed that the scanning speed is the leading parameter affecting the ratio of cladding track width to height, followed by powder feeding rate, while the laser power has the least on it as the *p*-value is far exceeding 0.05. It can be interpreted that with the decrease in scanning speed, the range of energy absorbed by the molten pool expanded, resulting in the widening of the cladding track width. Besides, the height of the cladding track heightens due to more powder being melted at a faster powder feeding rate. Therefore, the above reasons have a direct impact on the ratio of cladding track width to height. In addition, it can be found from Table 7 that the laser power and scanning speed have a significant effect on the fluctuation ratio, followed by the powder feeding rate. The powder can melt more fully on account of the powder obtaining sufficient energy with the increase of laser power and the decrease of scanning speed. As discussed above, the surface smoothness of the cladding track can be efficiently improved. As analyzed in the case of Table 7 and Figure 12, the effect order of each process parameter on the ratio of cladding track width to height and fluctuation ratio is $V_s > V_f > P$ and $V_s > P > V_f$. The main effect plot Figure 12 for *SNR* presents that the combination of the largest ratio of cladding track width to height and the lowest fluctuation ratio is $P5V_s5V_f1$ and $P4V_s1V_f4$, respectively.

Table 7. ANOVA results of $\lambda_{W/H}$ and λ_f.

Source	A_c					A_{HAZ}				
	P	***V_s***	***V_f***	**Error**	**Total**	***P***	***V_s***	***V_f***	**Error**	**Total**
DF	4	4	4	12	24	4	4	4	12	24
Seq SS	1.095	9.306	2.888	1.887	15.176	0.228	0.374	0.011	0.023	0.636
Adj SS	1.095	9.306	2.888	1.887		0.228	0.374	0.011	0.023	
Adj MS	0.274	2.326	0.722	0.157		0.057	0.094	0.003	0.002	
F-value	1.74	14.79	4.59			29.51	48.37	1.37		
p-value	0.206	0.000	0.018			0.000	0.000	0.300		

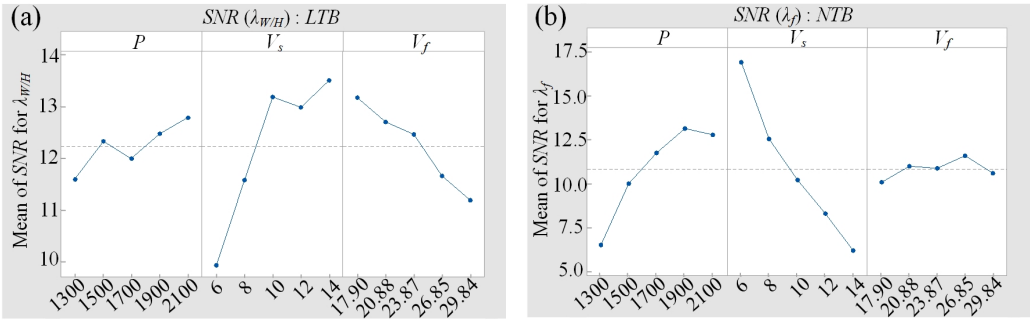

Figure 12. Main effect plots for the *SNR* analysis of (**a**) $\lambda_{W/H}$ and (**b**) λ_f.

Table 8 shows the ANOVA results for the cladding efficiency and powder utilization rate, and it can be seen that the *p*-values of each process parameter in the cladding efficiency are far less than 0.05. According to Equation (1), the cladding efficiency is positively correlated with the cladding track cross-section area and the scanning speed. As above discussed, the laser power, scanning speed, and powder feeding rate are the key factors affecting the cladding track cross-section area. Additionally, it can be seen from Table 8 that the influence degree of laser power and scanning speed on powder utilization rate is more remarkable than that of powder feeding rate. The powder utilization rate decrease is because that is limited by laser energy and the unmelted powder increase is caused by a larger powder feeding rate. From the analysis of Table 9 and Figure 13, it can be obtained that the impact order of each process parameter on the cladding efficiency and powder utilization rate is $P > V_s > V_f$. It can be observed from the main effect plot (Figure 13) that the combination of process parameters for the highest cladding efficiency and powder utilization are $P5V_s1V_f5$ and $P5V_s1V_f1$, respectively.

Table 8. ANOVA results of η_c and η_p.

Source	A_c					A_{HAZ}				
	P	***Vs***	***Vf***	**Error**	**Total**	***P***	***Vs***	***Vf***	**Error**	**Total**
DF	4	4	4	12	24	4	4	4	12	24
Seq SS	789.85	505.38	126.54	33.30	1455.07	0.398	0.247	0.036	0.035	0.716
Adj SS	789.85	505.38	126.54	33.30		0.398	0.247	0.036	0.035	
Adj MS	197.46	126.34	31.636	2.775		0.099	0.062	0.009	0.003	
F-value	71.15	45.52	11.40			33.66	20.87	3.04		
p-value	0.000	0.000	0.018			0.000	0.000	0.060		

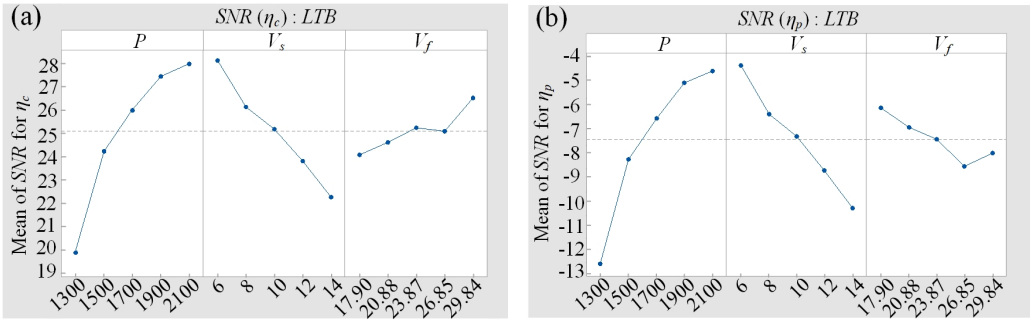

Figure 13. Main effect plots for the *SNR* analysis of (**a**) η_c and (**b**) η_p.

Table 9. Responses of *SNR* for A_c, A_{HAZ}, $\lambda_{W/H}$, λ_f, η_c, and η_p.

	A_c			A_{HAZ}			$\lambda_{W/H}$		
	P	***V_s***	***V_f***	***P***	***V_s***	***V_f***	***P***	***V_s***	***V_f***
1	0.221	12.568	4.442	−9.619	−15.198	−13.008	11.587	9.917	13.165
2	4.603	8.064	4.972	−11.696	−13.823	−13.307	12.324	11.568	12.699
3	6.369	5.191	5.609	−13.050	−12.616	−12.845	11.991	13.187	12.451
4	7.841	2.225	5.457	−13.894	−11.186	−12.237	12.475	12.981	11.653
5	8.352	−0.663	6.906	−15.022	−10.457	−11.884	12.783	13.307	11.181
Delta	8.131	13.231	2.464	5.403	4.740	1.43	1.196	3.590	1.983
Rank	2	1	3	1	2	3	3	1	2
	λ_f			η_c			η_p		
	P	*V_s*	*V_f*	*P*	*V_s*	*V_f*	*P*	*V_s*	*V_f*
1	6.491	16.886	10.053	19.851	28.130	24.071	−13.085	−4.535	−6.384
2	9.997	12.543	10.981	24.230	26.132	24.602	−8.586	−6.634	−7.198
3	11.720	10.192	10.864	25.992	25.191	25.244	−6.810	−7.605	−7.726
4	13.110	8.267	11.577	27.470	23.813	25.086	−5.288	−9.075	−8.898
5	12.745	6.175	10.588	27.981	22.263	26.535	−4.765	−10.685	−8.329
Delta	6.619	10.711	1.524	8.130	5.867	2.464	8.320	6.150	2.515
Rank	2	1	3	1	2	3	1	2	3

From the ANOVA above results, it can be concluded that the Taguchi method is only suitable for single-objective process optimization. As illustrated in Figures 11–13, the optimal parameters combination of the largest Ac, the smallest AHAZ, the largest $\lambda_{W/H}$, the lowest λ_f, the highest η_c and η_p are $P5V_s1V_f5$, $P1V_s5V_f5$, $P5V_s5V_f1$, $P4V_s1V_f4$, $P5V_s1V_f5$, and $P5V_s1V_f1$, respectively. Furthermore, it is observed that the optimal results corresponding to each response have significant differences. Therefore, in order to achieve multi-objective process optimization, the grey relational analysis method is adopted to further analyze the above optimization results [14,24,30].

3.2.2. The Grey Relational Analysis for Multi-Objective

Since each response has different evaluation angles on the cladding layer-forming characteristics, it is necessary to carry out dimensionless processing. Firstly, the response results are normalization processed, which calculation method is as follows Equation (5) [31], and the calculation results are shown in Table 10. Secondly, the grey correlation coefficient (GRC) is calculated according to the normalized results, as shown in Equation (6) [13]. Finally, the grey relational coefficient of each response is integrated into the grey relational grade (GRG) using Equation (7) [32], and the calculation results of GRC and GRG are listed in Table 11.

$$x_i(k) = \frac{y_i(k) - \min y_i(k)}{\max y_i(k) - \min y_i(k)} \tag{5}$$

where $x_i(k)$ is the normalization value for response k (k = 1, 2, . . . , 6) of experiment i (i = 1, 2, . . . , 25), $y_i(k)$ is the *SNR* for response k of experiment i, max $y_i(k)$ and min $y_i(k)$ are the maximum and minimum *SNR* results of the response k for all experiments.

$$GRC_i(k) = \frac{\min_i \left| x_i^0 - x_i(k) \right| + \xi \max_i \left| x_i^0 - x_i(k) \right|}{\left| x_i^0 - x_i(k) \right| + \xi \max_i \left| x_i^0 - x_i(k) \right|} \tag{6}$$

where $GRC_i(k)$ is the grey relational coefficient for response k of experiment i, x_i^0 is the ideal normalization value of experiment i, and ξ represents the distinguishing coefficient, and the value range is $0 < \xi < 1$. Considering *GRC* expresses the relationship between the actual

normalization and the ideal value, and the stability of the experiment, $x_i^0 = 1$, $\xi = 0.5$ are set in this research.

$$GRG_i = \frac{1}{m}\sum_{k=1}^{m} GRC_i(k) \quad (7)$$

where GRG_i is the grey relational grade for response k of experiment i, m is the number of responses, and $m = 6$ in this study.

Table 10. Results of Normalized calculation.

No.	x_i (k)					
	A_c	A_{HAZ}	$\lambda_{W/H}$	λ_f	η_c	η_p
1#	0.623	0.338	0.248	0.474	0.447	0.712
2#	0.251	0.489	0.594	0.301	0.082	0.245
3#	0.155	0.596	0.810	0.213	0.083	0.160
4#	0.020	0.835	0.235	0.164	0.000	0.000
5#	0.033	1.000	0.328	0.000	0.116	0.048
6#	0.752	0.232	0.218	0.694	0.636	0.807
7#	0.608	0.361	0.335	0.509	0.607	0.690
8#	0.451	0.497	0.713	0.359	0.517	0.527
9#	0.356	0.639	0.639	0.300	0.493	0.429
10#	0.000	0.634	1.000	0.165	0.067	0.321
11#	0.843	0.175	0.087	0.817	0.769	0.852
12#	0.691	0.296	0.258	0.576	0.728	0.735
13#	0.569	0.417	0.541	0.465	0.691	0.635
14#	0.288	0.466	0.957	0.312	0.392	0.651
15#	0.214	0.426	0.750	0.288	0.382	0.537
16#	0.922	0.109	0.101	1.000	0.886	0.901
17#	0.779	0.227	0.329	0.645	0.857	0.803
18#	0.521	0.287	0.805	0.457	0.619	0.878
19#	0.426	0.351	0.849	0.408	0.596	0.756
20#	0.322	0.443	0.961	0.294	0.540	0.616
21#	1.000	0.000	0.000	0.765	1.000	0.952
22#	0.696	0.074	0.681	0.633	0.736	1.000
23#	0.617	0.170	0.843	0.582	0.760	0.925
24#	0.488	0.293	0.839	0.411	0.687	0.764
25#	0.295	0.394	0.971	0.323	0.500	0.501

In summary, the laser power and scanning speed are the most influential factors on the grey relational grade in accordance with the *p*-value of ANOVA results, as listed in Table 12, while the powder feeding rate has a weak effect on it. Furthermore, from the main effect plot as shown in Figure 14 and the *SNR* response table for the grey relational grade (Table 13), it is illustrated that the influence order of each process parameter on *GRG* value is: $P > V_s > V_f$. In addition, the *GRG* value rises sharply with the laser power increases. When the scanning speed increases, the *GRG* value decreases rapidly and then slowly. While the influence of the powder feeding rate on the *GRG* value remains at a basically stable level, which is closely related to the laser energy density limiting the amount of effective powder melting. Finally, the optimal combination of process parameters is obtained according to the maximum mean of *SNR* for *GRG*, which is $P = 2100$ W, $V_s = 6$ mm/s, and $V_f = 17.90$ g/min.

Table 11. Grey relational analysis for responses.

No.	*GRC*						*GRG*		
	A_c	A_{HAZ}	$\lambda_{W/H}$	λ_f	η_c	η_p	Values	*SNR*	Rank
1#	0.570	0.430	0.613	0.487	0.475	0.634	0.535	−5.434	15
2#	0.400	0.495	0.552	0.417	0.353	0.399	0.436	−7.214	24
3#	0.372	0.553	0.725	0.388	0.353	0.373	0.461	−6.731	23
4#	0.338	0.751	0.395	0.374	0.333	0.333	0.421	−7.516	25
5#	0.341	1.000	0.427	0.333	0.361	0.344	0.468	−6.599	22
6#	0.668	0.394	0.390	0.620	0.579	0.722	0.562	−5.002	9
7#	0.561	0.439	0.429	0.505	0.560	0.617	0.518	−5.706	17
8#	0.477	0.499	0.635	0.438	0.509	0.514	0.512	−5.817	18
9#	0.437	0.580	0.580	0.417	0.497	0.467	0.496	−6.084	20
10#	0.333	0.577	1.000	0.375	0.349	0.424	0.510	−5.853	19
11#	0.761	0.377	0.354	0.732	0.684	0.772	0.613	−4.246	5
12#	0.618	0.415	0.403	0.541	0.648	0.653	0.546	−5.251	13
13#	0.537	0.462	0.521	0.483	0.618	0.578	0.533	−5.463	16
14#	0.412	0.483	0.921	0.421	0.451	0.589	0.546	−5.250	12
15#	0.389	0.466	0.667	0.413	0.447	0.519	0.483	−6.314	21
16#	0.865	0.359	0.357	1.000	0.814	0.834	0.705	−3.035	2
17#	0.693	0.393	0.427	0.585	0.777	0.717	0.599	−4.455	6
18#	0.511	0.412	0.720	0.480	0.568	0.804	0.582	−4.697	7
19#	0.466	0.435	0.768	0.458	0.553	0.672	0.559	−5.057	10
20#	0.424	0.473	0.928	0.415	0.521	0.566	0.554	−5.123	11
21#	1.000	0.333	0.333	0.681	1.000	0.912	0.710	−2.977	1
22#	0.622	0.351	0.610	0.576	0.655	1.000	0.636	−3.935	3
23#	0.566	0.376	0.761	0.545	0.676	0.870	0.632	−3.983	4
24#	0.494	0.414	0.756	0.459	0.615	0.679	0.570	−4.888	8
25#	0.415	0.452	0.945	0.425	0.500	0.500	0.540	−5.359	14

Table 12. ANOVA results of the *GRG*.

Source	*GRG*				
	P	V_s	V_f	**Error**	**Total**
DF	4	4	4	12	24
Seq SS	0.077	0.041	0.003	0.008	0.128
Adj SS	0.077	0.041	0.003	0.008	
Adj MS	0.019	0.010	0.001	0.001	
F-value	30.53	16.30	1.14		
p-value	0.000	0.000	0.384		

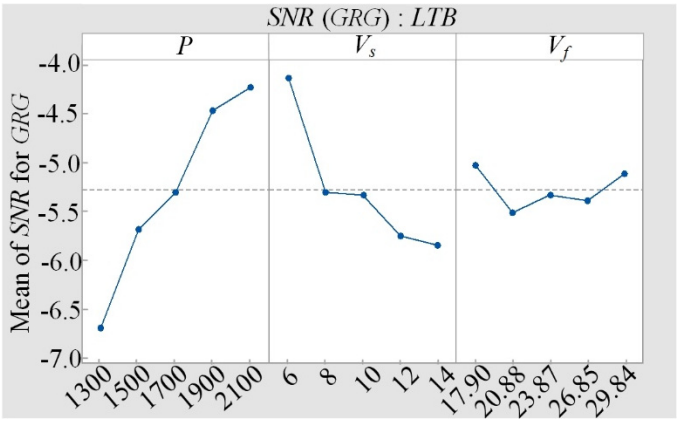

Figure 14. Main effect plot for the *SNR* analysis of the *GRG*.

Table 13. Responses for *SNR* of the *GRG*.

Level	P	V_s	V_f
1	−6.699	−4.139	−5.034
2	−5.692	−5.312	−5.514
3	−5.305	−5.338	−5.339
4	−4.437	−5.759	−5.396
5	−4.228	−5.850	−5.116
Delta	2.470	1.711	0.480
Rank	1	2	3

3.3. Experimental Verification

The optimal parameter combination $P5V_s1V_f1$ obtained by the above grey relational analysis is not included in the $L_{25}(5^3)$ Taguchi orthogonal experiment scheme. Therefore, additional experimental verification of the parameter combination is required. The calculation method of the grey correlation grade predicted value GRG_p is shown in Equation (8).

$$GRG_p = \overline{GRG_t} + \sum_{j=1}^{q} \left(GRG_j - \overline{GRG_t} \right) \quad (8)$$

where GRG_p is the predicted value of GRG; $\overline{GRG}$ is the total average value of GRG; GRG_j is the total average value of GRG at the optimal level of each process parameter j (j = 1, 2, 3); q represents the number of process parameters studied as 3. After calculation, the GRG_p value of the optimal process parameter combination is 0.706.

The experimental results show that the GRG value of the optimal process parameter combination $P5V_s1V_f1$ is 0.681, as shown in Table 14. The prediction accuracy is 96%, which is 0.260 higher than that of the initial parameter combination $P1V_s5V_f5$. The morphology of the optimal cladding track is shown in Figure 15. The surface of the cladding track is smooth without cracks, holes, and other obvious defects, which dramatically improves the surface forming quality compared with the initial parameters. Combined with Table 14 and Figure 15, the variations of grey correlation coefficients of the initial and optimal parameters can be compared more intuitively. The increase of heat affected zone area of the cladding track after optimization is caused by the increment of heat transferred from the laser beam and molten pool to the substrate caused by the increasing laser power and the decreasing scanning speed. The cross-section area, the ratio of width to height, cladding efficiency, and powder utilization rate of the optimal cladding track increased by 4.065 mm^2, 1.031, 19.032, and 70.3%, respectively, and the fluctuation ratio decreased by 60.9%. After optimization, the forming quality, processing efficiency, and cost economy of the cladding track are expected to be improved, which verifies the feasibility of combining the optimal process window with the grey correlation analysis method to optimize the process parameters of manufacturing the Co-based alloy cladding layer.

Table 14. Grey relational grades analysis of the initial and optimal parameters.

Evaluation Items	Initial Parameters	Optimal Parameters	
		Experiment	Prediction
	$P1V_s5V_f5$ (5#)	$P5V_s1V_f1$	$P5V_s1V_f1$
A_c (mm^2)	0.65	4.735	-
A_{HAZ} (mm^2)	2.37	7.282	-
$\lambda_{W/H}$	3.34	4.568	-
λ_f (%)	0.552	0.196	-
η_c (mm^3/s)	7.80	28.41	-
η_p (%)	0.152	0.868	-
GRG	0.421	0.681	0.706

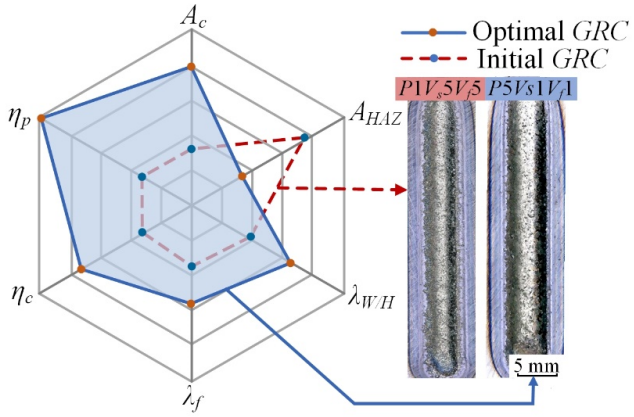

Figure 15. Redar chart of the optimal parameters $P5V_s1V_f1$ and initial parameters $P1V_s5V_f5$(5#).

Figure 16 shows the microstructure morphology of the single cladding track fabricated by the optimal parameter combination (P = 2100 W, V_s = 6 mm/s, V_f = 17.90 g/min). In Figure 16a, the dendrite evolution from the substrate to the top of the cladding layer is plane crystal, cellular crystal, columnar crystal, dendrite crystal, and equiaxed crystal. As shown in Figure 16b, a white-bright fusion zone with a thickness of about 2–3 μm is formed at the interface, indicating that the substrate and cladding layer achieve good metallurgical bonding. The temperature gradient G at the interface is maximum and the solidification rate R of the molten pool is almost zero, resulting in an extremely high value of G/R, thus the white-bright zone is composed of planar crystals. The temperature gradient G decreases gradually along the solidification direction of the molten pool, the solidification rate R increases, the G/R decreases gradually, and the formation of cellular crystal begins. It can be seen from Figure 16c that the middle of the cladding layer is composed of columnar crystals and dendrites growing perpendicular to the substrate. With the upward movement of the solidification interface, the temperature gradient decreases gradually, resulting in the transition from planar crystals to columnar crystals. The microstructure of the upper middle region is shown in Figure 16d, the solidification rate R is accelerated via the increasing heat dissipation in the surrounding atmosphere [31], and the massive fine equiaxed crystals are induced. The G/R decreases and the preceding melt supercooling increases gradually as the crystallization proceeds to the top of the cladding layer. The supercooling of columnar crystals is higher than the nucleation cooling rate, so the solidification interface grows in the form of dendrites. The crystals grow freely in the undercooled melt via the nucleation that occurs in front of the solid-liquid interface and finally form anisotropic equiaxial dendrites [33]. The microstructure of the cladding layer is dense, the crystals are uniformly distributed, and there are no obvious defects such as pores and cracks inside, which proves that the optimized internal cladding layer has good forming quality.

In Figure 17, the distribution of elements from the cladding layer to the substrate was characterized by EDS. The surface scanning results of EDS in Figure 17d–g show that the cladding layer is rich in Co, Cr, and W elements, and the substrate is mainly composed of Fe elements, with uniform distribution of elements and no segregation. Co and Cr are mainly distributed in the cladding layer, and all elements have a certain degree of interfacial diffusion, among which the diffusion of the W element is evident. The energy spectrum analysis results in Figure 17c showing that the Fe element accounts for the largest proportion of 51.6%, followed by Co and Cr elements. During the transition from the cladding layer to the substrate, the contents of Co and Fe decreased and increased sharply, respectively, while the content of Cr decreased rapidly, as shown in Figure 17h, which is closely related to the high cooling rate of the laser cladding process to minimize the diffusion between elements [34].

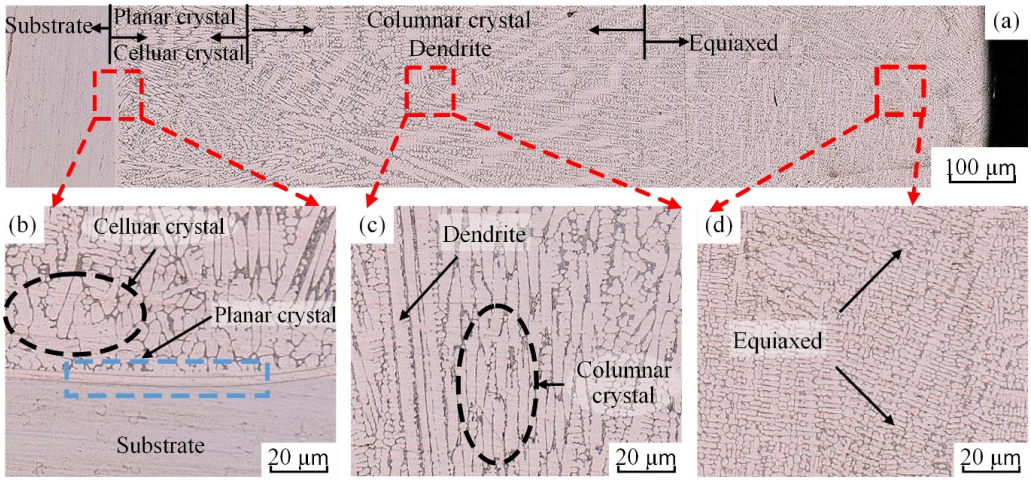

Figure 16. Microstructure characteristics of cladding layer with optimal parameter $P5V_s1V_f1$: (**a**) Microstructure evolution; (**b**–**d**): Crystal characteristics from bottom to top of cladding layer.

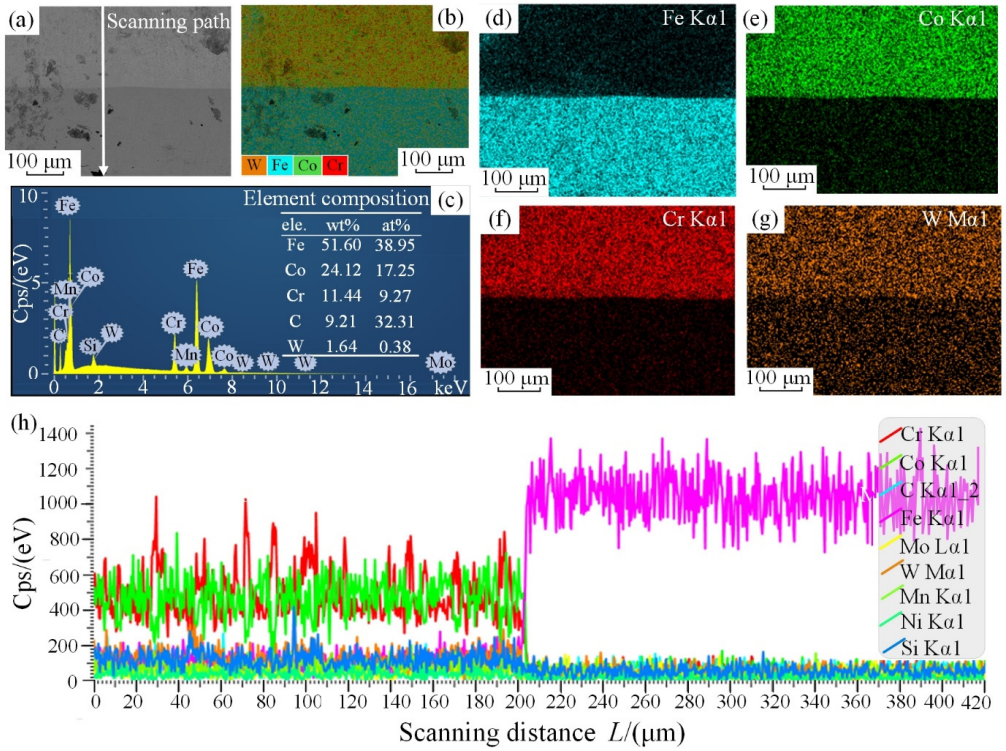

Figure 17. EDS results of the cladding layer to substrate: (**a**) SEM image; (**b**) EDS layered image; (**c**) Elemental composition; (**d**–**g**) Corresponding elements distribution of Fe, Co, Cr, and W; (**h**) Line scanning element changes.

The XRD pattern presents the phase composition of the Co-based alloy cladding layer, as shown in Figure 18. The laser beam irradiation melts the Co-based powder, and a series of chemical reactions occur between the elements resulting in the formation of Cr_7C_3, CoC_X, fcc-Co, and WC phases. The presence of Ni in the cladding powder plays a role in stabilizing the face-centered cubic lattice structure and the cooling rate of the cladding layer is extremely fast, which mutually restricts the fcc-Co transformation of the face-centered cubic structure and increases the toughness and corrosion resistance of the cladding layer [35]. Meanwhile, the hard carbide phases such as Cr_7C_3, CoC_X, and WC are formed, which effectively improves the hardness of the cladding layer [36].

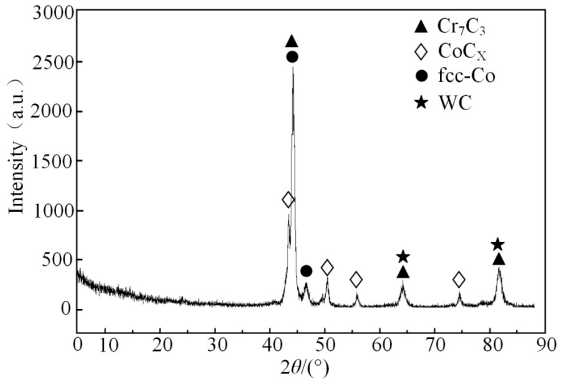

Figure 18. XRD pattern of Co-base alloy cladding layer.

4. Conclusions

(1) Considering the cross-section area of the cladding track, cladding efficiency, and powder utilization rate, the optimal process window of the Co-based alloy cladding layer was constructed. The optimal process parameter interval was determined as: P = 1300–2100 W, V_s = 6–14 mm/s and V_f = 17.90–29.84 g/min. The ANOVA results showed that the cross-section area and cladding efficiency were correlated with laser power, scanning speed, and powder feeding rate. The powder feeding rate had an inconspicuous effect on the fluctuation ratio, powder utilization rate, and heat-affected zone area. The scanning speed and powder feeding rate had a significant influence on the ratio of cladding track width to height.

(2) The optimal process parameters were determined by grey correlation analysis as follows: P = 2100 W, V_s = 6 mm/s and V_f = 17.90 g/min. It was concluded that the influence order of laser process parameters on the forming characteristics of the cladding track is: $P > V_s > V_f$. The *GRG* value of the optimal process parameter combination $P5V_s1V_f1$ was 0.681, and the prediction accuracy was 96%, which was 0.260 higher than that of the initial parameter combination $P1V_s5V_f5$.

(3) The cross-section area, the ratio of cladding track width to height, cladding efficiency, and powder utilization rate of the optimal cladding track increased by 4.065 mm^2, 1.031, 19.032, and 70.3%, respectively, and the fluctuation ratio decreased by 60.9%. The forming characteristics of the optimized cladding track were favorable, and the metallurgical bonding was formed with the substrate. The elements were evenly distributed without segregation, and the reinforcing phases of Cr_7C_3, CoC_X, and WC were precipitated from the cladding layer. The forming quality, processing efficiency, and cost economy of the optimized cladding track have been expected to improve effectively.

Author Contributions: Conceptualization, N.L. and C.G.; methodology, C.G.; validation, W.D., J.Z. (Jianhua Zhai) and G.Z.; formal analysis, H.Y.; investigation, H.Y. and N.L.; resources, C.G., J.Z. (Jianzhuo Zhang) and G.Z.; writing—original draft preparation, N.L. and C.G.; writing—review and editing, C.G. All authors have read and agreed to the published version of the manuscript.

Funding: This research is supported by the National Natural Science Foundation of China (Grant Nos. U1908222, 52174116, and 52204169), the Project supported by the discipline innovation team of Liaoning Technical University (Grant Nos. LNTU20TD-15 and LNTU20TD-28).

Institutional Review Board Statement: Not applicable.

Informed Consent Statement: Not applicable.

Data Availability Statement: Not applicable.

Conflicts of Interest: The authors declare no conflict of interest.

References

1. Gao, W.; Wang, S.C.; Hu, K.K.; Jiang, X.Z.; Yu, H.Y.; Sun, D.B. Effect of laser cladding speed on microstructure and properties of titanium alloy coating on low carbon steel. *Surf. Coat. Technol.* **2022**, *451*, 129029. [CrossRef]
2. Li, Y.T.; Wang, K.M.; Fu, H.G.; Guo, X.Y.; Lin, J.N. Microstructure and wear resistance of in-situ TiC reinforced AlCoCrFeNi-based coatings by laser cladding. *Appl. Surf. Sci.* **2022**, *585*, 152703. [CrossRef]
3. Bax, B.; Rajput, R.; Kellet, R.; Reisacher, M. Systematic evaluation of process parameter maps for laser cladding and directed energy deposition. *Addit. Manuf.* **2018**, *21*, 487–494. [CrossRef]
4. Yue, H.T.; Lv, N.; Guo, C.G.; Zhao, L.J.; Li, Q.; Zhang, J.Z.; Zhang, Y. Microstructure and mechanical properties of TiC/FeCrSiB coating by laser additive remanufacturing on shearer spiral blade. *Surf. Coat. Technol.* **2022**, *431*, 128043. [CrossRef]
5. Souza, N.D.; Ravichandran, S.; Donovan, S.; Daum, P.; Morrell, R.; Nye, Z.; Lancaster, R.J. On the design optimisation of direct energy deposited support structures to repair aero-engine turbine segments. *Addit. Manuf.* **2022**, *56*, 102905.
6. Thakare, J.G.; Pandey, C.; Mahapatra, M.M.; Mulik, R.S. Thermal Barrier Coatings—A State of the Art Review. *Met. Mater. Int.* **2021**, *27*, 1947–1968. [CrossRef]
7. Xiao, Q.; Li, S.Y.; Yang, W.B.; Yang, C.H.; Chen, D.Y.; Ding, H.H.; Wang, W.J. High-temperature tribological properties of coatings repaired by laser additive manufacturing on railway wheel tread damage. *Wear* **2023**, *520–521*, 204674. [CrossRef]
8. Ding, H.H.; Mu, X.P.; Zhu, Y.; Yang, W.B.; Xiao, Q.; Wang, W.J.; Liu, Q.Y.; Guo, J.; Zhou, Z.R. Effect of laser claddings of Fe-based alloy powder with different concentrations of WS2 on the mechanical and tribological properties of railway wheel. *Wear* **2022**, *488–489*, 204174. [CrossRef]
9. Sun, F.Z.; Cai, K.Q.; Li, X.X.; Pang, M. Research on Laser Cladding Co-Based Alloy on the Surface of Vermicular Graphite Cast Iron. *Coatings* **2021**, *11*, 1241. [CrossRef]
10. Gao, Q.; Liu, H.; Chen, P.J.; Liu, X.H.; Yang, H.F.; Hao, J.B. Multi-objective optimization for laser cladding refractory MoNbTiZr high-entropy alloy coating on Ti6Al4V. *Opt. Laser Technol.* **2023**, *161*, 109220. [CrossRef]
11. Meng, G.R.; Zhu, L.D.; Zhang, J.D.; Yang, Z.C.; Xue, P.S. Statistical analysis and multi-objective process optimization of laser cladding TiC-Inconel718 composite coating. *Optik* **2021**, *240*, 166828. [CrossRef]
12. Wu, S.; Liu, Z.H.; Huang, X.F.; Wu, Y.F.; Gong, Y. Process parameter optimization and EBSD analysis of Ni60A-25% WC laser cladding. *Int. J. Refract. Met. Hard Mater.* **2021**, *101*, 105675. [CrossRef]
13. Xu, Z.Y.; Yuan, J.F.; Wu, M.Y.; Arif, A.F.M.; Li, D.Y. Effect of laser cladding parameters on Inconel 718 coating performance and multi-parameter optimization. *Opt. Laser Technol.* **2023**, *158*, 108850. [CrossRef]
14. Deng, D.W.; Li, T.S.; Huang, Z.Y.; Jiang, H.; Yang, S.H.; Zhang, Y. Multi-response optimization of laser cladding for TiC particle reinforced Fe matrix composite based on Taguchi method and grey relational analysis. *Opt. Laser Technol.* **2022**, *153*, 108259. [CrossRef]
15. Guo, C.G.; Lv, N.; Yue, H.T.; Li, Q.; Zhang, J.Z. Laser additive remanufacturing parameters optimization and experimental study of heavy-duty sprocket. *Int. J. Adv. Manuf. Technol.* **2022**, *118*, 3789–3800. [CrossRef]
16. Ilanlou, M.; Razavi, S.R.; Nourollahi, A.; Hosseini, S.; Haghighat, S. Prediction of the geometric characteristics of the laser cladding of Inconel 718 on the Inconel 738 substrate via genetic algorithm and linear regression. *Opt. Laser Technol.* **2022**, *156*, 108507. [CrossRef]
17. Nabhani, M.; Razavi, S.R.; Barekat, M. An empirical-statistical model for laser cladding of Ti-6Al-4V powder on Ti-6Al-4V substrate. *Opt. Laser Technol.* **2018**, *100*, 265–271. [CrossRef]
18. Barekat, M.; Razavi, S.R.; Ghasemi, A. Nd:YAG laser cladding of Co–Cr–Mo alloy on γ-TiAl substrate. *Opt. Laser Technol.* **2016**, *80*, 145–152. [CrossRef]
19. Cui, C.; Wu, M.P.; Miao, X.J.; Gong, Z.S.; Zhao, Y.L. The effect of laser energy density on the geometric characteristics, microstructure and corrosion resistance of Co-based coatings by laser cladding. *J. Mater. Res. Technol.* **2021**, *15*, 2405–2418.
20. Zhou, J.L.; Kong, D.J. Friction–wear performances and oxidation behaviors of Ti3AlC2 reinforced Co–based alloy coatings by laser cladding. *Surf. Coat. Technol.* **2021**, *408*, 126816. [CrossRef]
21. Cui, C.; Wu, M.; He, R.; Gong, Y.L.; Miao, X.J. Investigation on the columnar-to-equiaxed transition and corrosion behavior in multi-track Stellite-6 coating fabricated by laser cladding. *Mater. Chem. Phys.* **2022**, *291*, 126681. [CrossRef]
22. Yang, Z.Y.; Jian, Y.X.; Chen, Z.H.; Qi, H.J.; Huang, Z.F.; Huang, G.S.; Xing, J.D. Microstructure, hardness and slurry erosion-wear behaviors of high-speed laser cladding Stellite 6 coatings prepared by the inside-beam powder feeding method. *J. Mater. Res. Technol.* **2022**, *19*, 2596–2610. [CrossRef]
23. Shao, J.Y.; Yu, G.; He, X.L.; Li, S.X.; Li, Z.X.; Wang, X. Process maps and optimal processing windows based on three-dimensional morphological characteristics in laser directed energy deposition of Ni-based alloy. *Opt. Laser Technol.* **2021**, *142*, 107162. [CrossRef]
24. Lian, G.F.; Zhang, H.; Zhang, Y.; Tanaka, M.L.; Chen, C.R.; Jiang, J.B. Optimizing Processing Parameters for Multi-Track Laser Cladding Utilizing Multi-Response Grey Relational Analysis. *Coatings* **2019**, *9*, 356. [CrossRef]
25. Yang, B.; Lai, Y.B.; Yue, X.; Wang, D.Y.; Zhao, Y.H. Parametric Optimization of Laser Additive Manufacturing of Inconel 625 Using Taguchi Method and Grey Relational Analysis. *Scanning* **2020**, *2020*, 9176509. [CrossRef]
26. Songur, F.; Arslan, E.; Dikici, B. Taguchi optimization of PEO process parameters for corrosion protection of AA7075 alloy. *Surf. Coat. Technol.* **2022**, *434*, 128202. [CrossRef]

27. Liu, Y.; Liu, C.; Liu, W.S.; Ma, Y.Z.; Tang, S.W.; Liang, C.P.; Cai, Q.S.; Zhang, C. Optimization of parameters in laser powder deposition AlSi10Mg alloy using Taguchi method. *Opt. Laser Technol.* **2019**, *111*, 470–480. [CrossRef]
28. Yadav, R.; Pandey, C.; Mahapatra, M.M.; Mulik, R.S. Study on Effect of Process Variables on Distributed Compositional Characteristics in Metallurgically and Mechanically Bonded Claddings. *Trans. Indian Inst. Met.* **2017**, *70*, 1805–1815. [CrossRef]
29. Guo, C.G.; He, S.Z.; Yue, H.T.; Li, Q.; Hao, G.B. Prediction modelling and process optimization for forming multi-layer cladding structures with laser directed energy deposition. *Opt. Laser Technol.* **2021**, *134*, 106607. [CrossRef]
30. Chang, Y.Y.; Qiu, J.R.; Hwang, S.J. Multi-objective optimization of directed energy deposition process by using Taguchi-Grey relational analysis. *Int. J. Adv. Manuf. Technol.* **2022**, *120*, 7547–7563. [CrossRef] [PubMed]
31. Lian, G.F.; Xiao, S.H.; Zhang, Y.; Jiang, J.B.; Zhan, Y.J. Multi-objective optimization of coating properties and cladding efficiency in 316L/WC composite laser cladding based on grey relational analysis. *Int. J. Adv. Manuf. Technol.* **2021**, *112*, 1449–1459. [CrossRef]
32. Yu, T.B.; Yang, L.; Zhao, Y.; Sun, J.Y.; Li, B.C. Experimental research and multi-response multi-parameter optimization of laser cladding Fe313. *Opt. Laser Technol.* **2018**, *108*, 321–332. [CrossRef]
33. Yue, H.T.; Lv, N.; Guo, C.G.; Zhao, L.J.; Li, Q.; Zhang, J.Z.; Zhang, Y. Microstructure evolution and defect characteristics of multilayer Fe-Cr alloy coatings fabricated by laser melting deposition. *Opt. Laser Technol.* **2023**, *158*, 108802. [CrossRef]
34. Guimaraes, B.; Guedes, A.; Fernandes, C.M.; Figueiredo, D.; Bartolomeu, F.; Miranda, G.; Silva, F.S. WC-Co/316L stainless steel joining by laser powder bed fusion for multi-material cutting tools manufacturing. *Int. J. Refract. Met. Hard Mater.* **2023**, *112*, 106140. [CrossRef]
35. Wang, L.; Mao, J.Z.; Xue, C.G.; Ge, H.H.; Dong, G.; Zhang, Q.L.; Yao, J.H. Cavitation-Erosion behavior of laser cladded Low-Carbon Cobalt-Based alloys on 17-4PH stainless steel. *Opt. Laser Technol.* **2023**, *158*, 108761. [CrossRef]
36. Chang, W.; Xiao, G.C.; Zhang, H.; Chen, H.; Yi, M.D.; Zhang, J.J.; Chen, Z.Q.; Xu, C.H. Microstructure and properties of graphene reinforced co-based composite coating by laser cladding. *Surf. Coat. Technol.* **2023**, *453*, 129139. [CrossRef]